Journal of Materials Chemistry C

ROYAL SOCIETY OF CHEMISTRY

PAPER

Published on 31 July 2026
Licensed under CC-BY 4.0

Check for updates

Cite this: DOI: 10.1039/d6tc01511e

A multiscale perspective on the surface functional properties of nanostructured metal-oxide gas sensors

Elena Spagnoli, *[ab] Arianna Rossi, [b] Vincenzo Guidi, [b] Elena Ghedini, [c] Michela Signoretto, [c] Alessia Giordana, [d] Giuseppina Cerrato, [d] Stefano Caramori, [ef] Anna Ianniello[e] and Barbara Fabbri [b]

Chemoresistive gas sensing is intrinsically multiscale, with macroscopic device performance emerging from molecular surface reactions coupled to charge transport across nanostructured networks. However, the causal relationships linking surface chemistry to device-level response remain poorly defined, limiting predictive sensor design. Here, we establish a multiscale, *operando* framework that correlates surface functional chemistry with the electrical response of WO_3-based sensors for D-limonene detection. By integrating temperature-dependent electrical measurements with NH_3-TPD, FT-IR spectroscopy using 2,6-dimethylpyridine, and *operando* DRIFTS under realistic operating conditions, we resolve structure–property–function relationships that are typically inaccessible using conventional *ex situ* approaches. Surface acidity emerges as a decisive functional descriptor: optimal sensing performance coincides with the highest density of acidic sites within a characteristic operating temperature window. Coordinatively unsaturated W^{6+} centers are identified as active sites for C=C bond activation in D-limonene, enabling pronounced sensor responses at a relatively low temperature of 200 °C. *Operando* DRIFTS further reveals the direct participation of surface hydroxyl groups in the sensing reaction, while moderate humidity does not alter the dominant reaction pathway, underscoring the robustness of the mechanism under realistic conditions. By explicitly linking surface Lewis acidity and hydroxyl chemistry to macroscopic sensing behaviour, this work advances chemoresistive gas sensing as a mechanism-driven, predictive discipline. More broadly, the multiscale *operando* strategy introduced here provides a generalizable blueprint for the rational design of functional metal-oxide interfaces.

Received 11th May 2026,
Accepted 21st July 2026

DOI: 10.1039/d6tc01511e

rsc.li/materials-c

1. Introduction

Nanostructured metal-oxide (MOX) sensing films used in chemoresistive gas sensors represent a paradigmatic class of functional materials in which macroscopic device properties emerge from processes occurring across multiple, strongly coupled length scales.

At the microscale, gas sensing originates from adsorption, surface reactions, and charge-transfer events at specific surface sites, which generate local electronic perturbations. At the mesoscale, these perturbations propagate through the nanostructured sensing layer by modulating band bending, intergrain potential barriers, and charge-percolation pathways. Their collective effects ultimately produce the measurable resistance change observed at the macroscale. As such, chemoresistive sensing is intrinsically a micro–meso–macro multiscale phenomenon, in which the mesoscale charge-transport regime provides the physical transduction pathway linking surface chemistry to the device-level response (Fig. 1). The three scales are closely dependent: variations in operating conditions, such as temperature and gas composition, simultaneously affect surface chemistry, charge transport, and device-level performance.[1,2]

Establishing explicit causal links across these scales is essential for advancing chemoresistive sensing beyond empirical optimization toward mechanism-driven materials design. Nevertheless, achieving this remains a major challenge.

[a] National Research Council (CNR), Institute for Nanostructured Materials (ISMN), Via P. Gobetti 101, Bologna 40129, Italy. E-mail: elena.spagnoli@cnr.it
[b] Department of Physics and Earth Sciences, University of Ferrara, Via Saragat 1/C, Ferrara 44122, Italy
[c] Catmat Lab, Department of Molecular Sciences and Nanosystems, Venice Ca' Foscari University and INSTM Ruve, Via Torino 155, Venice 30172, Italy
[d] Centre and INSTM RUTo, Chemistry Department and NIS Interdept, University of Turin, Via P. Giuria 7, Turin 10125, Italy
[e] Department of Chemical, Pharmaceutical and Agricultural Sciences, University of Ferrara, via Fossato di Mortara 17, Ferrara 44121, Italy
[f] National Interuniversity Consortium of Materials Science and Technology (INSTM), Ferrara Research Unit, Via Luigi Borsari 46, 44121 Ferrara, Italy

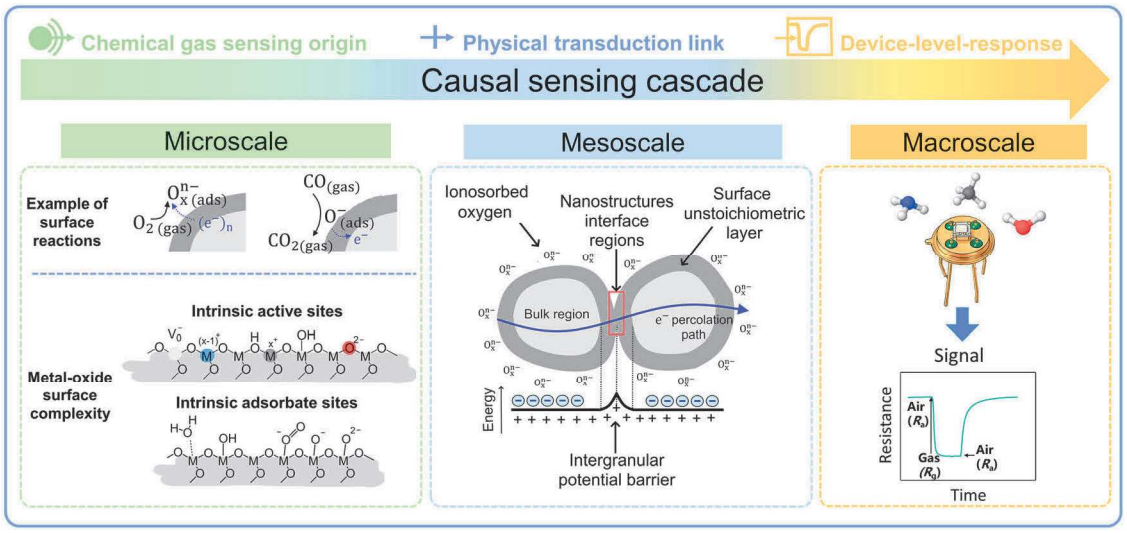


Fig. 1 Mechanistic multiscale framework for chemoresistive gas sensing.

While semiconductor band theory successfully describes charge transport at the mesoscale and macroscale, it often treats surface chemistry at the microscale in a simplified or phenomenological manner. Indeed, general models classically exemplified surface-induced changes in electrical resistance through oxygen ionosorption and subsequent gas–surface reactions, modulating band bending and intergrain barrier heights.[3] These descriptions rarely capture the chemical specificity of real sensing processes. In practice, MOX surfaces host heterogeneous and temperature-dependent populations of Lewis and Brønsted acid–base sites, hydroxyl groups, oxygen species, and defects, whose nature and reactivity critically determine sensor performance.[4] The identity, density, and reactivity of these sites ultimately govern sensor response kinetics, selectivity, sensitivity, and stability. The microscale thus represents the origin of the entire sensing cascade: only by elucidating the nature of surface sites, and their participation in reactions with target molecules and potential interferents, can synthetic strategies be rationally devised to tune material properties toward specific sensing applications.

In this work, we propose an integrated multiscale strategy that explicitly connects microscale surface chemistry to macroscale sensing performance. Each experimental technique is deliberately designed to probe a specific length scale while remaining explicitly connected to the others. Electrical characterization provides the macroscale readout of the sensing function, identifying operating regimes (*e.g.* sensor working temperature or humidity levels) in which the device response undergoes qualitative or quantitative changes. However, this information alone does not reveal the microscopic origins of such regimes. Temperature-programmed desorption (TPD) and FT-IR spectroscopy with probe molecules are therefore employed to investigate the microscale, enabling a temperature-resolved analysis of the chemical nature, strength, and distribution of surface acid–base sites that potentially participate in gas detection. These *ex situ* measurements define the population of candidate active sites at specific operating temperatures but do not capture their actual involvement under sensing conditions or the role of reactive oxygen species typically present on MOX surfaces. Bridging this gap requires an *operando* approach capable of simultaneously tracking surface chemistry and electrical transduction. *Operando* DRIFTS fulfills this role by monitoring the formation and consumption of surface species during gas exposure while the sensor is actively operating under thermal or photoactivation.[5–7] In this way, it provides the missing causal link between microscale reaction pathways and the macroscale resistance response. The integration of these complementary techniques thus transforms a set of otherwise disconnected observations into a coherent multiscale picture of the sensing mechanism. More broadly, the proposed strategy provides a general blueprint for the rational, mechanism-driven design of next-generation gas-sensing materials.

To demonstrate the approach, we selected WO_3 not because it represents a novelty in chemoresistive sensing, but precisely because it is a benchmark material whose behaviour is notoriously difficult to interpret without in-depth structural and chemical analysis. Since its first application in chemoresistive gas sensing in 1967,[8] WO_3 has become one of the most extensively investigated MOX materials, alongside SnO_2 and ZnO, and has been the subject of several dedicated reviews.[9–14] This sustained interest stems from the remarkable tunability of WO_3 sensing properties, which can be finely tailored by the synthesis route and annealing treatments through their influence on crystal structure, morphology, and surface reactivity. Indeed, despite its simple stoichiometry, WO_3 exhibits multiple temperature-dependent polymorphs due to structural distortions and phase transitions of its ideal ReO_3-type cubic lattice.[15–17] In addition, oxygen deficiencies, ranging from isolated vacancies to ordered defect arrangements approaching Magnéli-type substoichiometric compositions (*e.g.*, $WO_{2.9}$), introduce further electronic and structural complexity. Morphology and grain size further modulate surface-site density and reaction kinetics.[18] Such intertwined structural and chemical variables

 This journal is © The Royal Society of Chemistry 2026

make WO_3 an ideal yet demanding platform to investigate how microscale features propagate through the mesoscale architecture to determine macroscale sensing behaviour.

As a chemically demanding and technologically relevant analyte, D-limonene was chosen as a test case for the proposed multiscale framework. This volatile organic compound (VOC) is increasingly relevant in industrial process monitoring, food quality control, agricultural emission assessment, and non-invasive medical diagnostics, where it has been investigated as a potential biomarker in breath analysis.[19–24]

Previous studies have independently demonstrated the suitability of WO_3 for D-limonene detection. Weber *et al.* demonstrated the capability of WO_3-based gas sensors to detect limonene in trace concentrations (20–500 ppb),[24] while Rossi *et al.* reported a systematic comparison of functional metal oxides, including ZnO, SnO_2, noble-metal-decorated variants, and mixed oxides, and identified WO_3 as the most responsive and selective material for D-limonene detection.[25] Despite the reproducible macroscopic performance of WO_3, the mechanisms underlying its sensitivity to limonene remain unresolved.

From a physicochemical standpoint, D-limonene constitutes a molecular stress test system for chemoresistive sensing. Its structure, featuring reactive C=C double bonds, allylic hydrogen atoms, and pronounced steric bulk within a cyclic terpene backbone, introduces multiple potential adsorption configurations and reaction pathways. This complexity promotes competitive adsorption phenomena involving Lewis and Brønsted surface sites, hydroxyl groups, and ionosorbed oxygen species. Consequently, the interaction of D-limonene with WO_3 surfaces cannot be adequately described by simplified oxygen-ionosorption models alone, but instead requires a chemically resolved analysis of site identity, distribution, and reactivity.

Mechanistic investigations were also conducted under identical operating conditions using acetone, selected as a representative interfering ketone, and NO_2, employed as an oxidizing probe molecule to investigate intrinsic electron-donor sites, such as partially reduced metal cations and oxygen vacancies.[4]

By resolving how the operating temperature reshapes surface-site populations and reaction pathways at the microscale, and how these modifications are transduced through the nanostructured WO_3 network to yield macroscopic resistance changes, this work elucidates the multiscale functional mechanisms underlying D-limonene detection. Beyond this specific case, the conceptual and methodological framework developed here establishes transferable design principles for MOX-based sensing of alkenes and structurally related volatile compounds.

2. Results

2.1 Structural and baseline sensing properties of nanoflaked WO_3 for D-limonene detection

The morphological, structural, and chemical properties of the nanoflaked WO_3 employed in this study were previously reported in detail.[15] Here, the key features are briefly summarized to establish the structural and functional baseline for the multiscale investigation.

The material consists of nanoflakes with thicknesses of 20–30 nm and lateral dimensions ranging from 200 nm to 1 μm. As shown in Fig. S1, the surface is characterized by a high density of steps, kinks, and dislocations, indicative of a defect-rich morphology. Nitrogen adsorption–desorption measurements yield a Brunauer–Emmett–Teller (BET) specific surface area of 12.11 $m^2\ g^{-1}$ and an average pore size of 20.4 nm, confirming the porous architecture of the sensing layer.

X-ray diffraction analysis reveals that the powder at room temperature (RT) is predominantly monoclinic WO_3 ($\approx$98.6 wt%, space group $P2_1/n$), with a minor fraction ($\approx$1.4 wt%) of hexagonal WO_3 (space group $P6_3/mcm$). X-ray photoelectron spectroscopy identifies W and O as the main surface constituents. High-resolution W 4f spectra indicate that tungsten is predominantly present as W^{6+}, with no detectable contribution from W^{5+} species under ambient conditions.

The gas-sensing performance of nanoflaked WO_3 was previously demonstrated for detection of D-limonene, highlighting its high sensitivity and selectivity toward this target VOC and providing the basis for the present study.[25] Cross-selectivity measurements showed that the response to 5 ppm of limonene was almost unaffected by ethanol and acetaldehyde, while acetone decreased the sensor response by approximately four times. On this basis, in this work, *operando* DRIFTS measurements were also performed under acetone exposure.

A pronounced dependence of the sensor response on operating temperature was observed between 200 °C and 400 °C, with 200 °C identified as the optimal working condition.[25] At 300 °C, the response nearly halved;[25] accordingly, the surface properties of nanoflaked WO_3 were investigated at 200 °C and 300 °C as representative regimes exhibiting marked changes in the device's response. A second critical operating regime was identified in the low-humidity range (2–20% RH), where the conductance in wet increased from 0.2 to 0.8 mS, while the response to 0.5 ppm of D-limonene decreased from 7.5 to 2.5.[25] In contrast, the response remained nearly humidity-independent between 20 and 70% RH (RT conditions inside the reaction chamber).[25] Based on this behaviour, *operando* DRIFTS measurements were performed at 13% RH at 30 °C to assess whether the observed variation in sensing response could be related to changes in the reaction pathway induced by surface hydroxylation.

Despite the reproducible macroscopic performance of WO_3 as a robust and promising platform for limonene sensing, the physicochemical mechanisms underlying its selectivity and pronounced temperature dependence remain unresolved. The following sections address this issue through a comprehensive multiscale approach combining temperature-programmed analyses, probe-molecule spectroscopy, and *operando* DRIFTS coupled with electrical measurements.

2.2 Acid–base properties

TPR measurement was performed to understand the oxidation state of W at the sensor operating temperature, while TPD with

CO_2 and NH_3, used as probe molecules, investigated the acidic or basic nature of the material surface.

In the TPR profile, as shown in Fig. S2, the WO_3 powder exhibits three main reduction peaks, which according to the literature can be attributed to the following reduction steps: (i) the first at 620 °C ($WO_3 \rightarrow W_{20}O_{58}$), (ii) a sharp peak at 775 °C ($W_{20}O_{58} \rightarrow WO_2$) and (iii) two last peak at a higher temperature ($WO_2 \rightarrow W$).[26]

The desorption analyses in the programmed temperature of CO_2 were carried out on the sample activated at 300, 200, and 50 °C (Fig. S3). Regardless of the experimental conditions used, completely flat profiles were obtained, indicating the absence of interaction between the gas and the oxide surface and the consequent absence of identifiable basic sites.

On the other hand, Fig. 2 displays that NH_3 TPD profiles are strongly influenced by the temperature of sample activation. At 50 °C, the profile was flat, indicating the absence of acid sites. When the activation temperature was increased to 200 °C, the TPD profile exhibited a pronounced peak at 300 °C, accompanied by a shoulder at approximately 325 °C, along with a less intense peak at 395 °C. Increasing the activation temperature to 300 °C resulted in the disappearance of the peaks at 300 °C and 325 °C, while a broad, less intense peak centered at approximately 370 °C emerged.

2,6-Dimethylpyridine (2,6-DMP) uptake was used as a complementary technique to NH_3 TPD to reveal the presence of acidic sites that differ either in nature (*i.e.*, Lewis or Brønsted) and/or in acidic strength.[27] For WO_3 activated at 200 °C, at a maximum pressure (~4 torr) (Fig. 3a, solid line), the strongest signals are represented by the two bands at 1594 cm^{-1} and 1580 cm^{-1}, ascribable to H-bonded and physisorbed 2,6-DMP molecules (Fig. 3c, orange star), respectively, besides two bands that are located at 1642 cm^{-1} and 1627 cm^{-1}, due to 2,6-$DMPH^+$ held to the surface, indicating the presence of Brønsted (B) acid sites (Fig. 3c, purple star). Upon outgassing (Fig. 3a, short dash line), the overall intensity of the envelope at lower wavenumbers drastically decreases, as expected for the elimination of physisorbed/weakly held species, whereas a signal at 1613 cm^{-1} remains still observable. This signal can be ascribed to 2,6-DMP molecules interacting with coordinatively unsaturated W^{6+} cations (Fig. 3c, green star) and the high frequency suggests the presence of Lewis (L) acid sites with medium strength.[28] The spectral features of 2,6-$DMPH^+$ species remain strong, with only a partial modification in intensity and profile as well, indicating the presence of medium-strength B acid sites. When the sample is activated at 300 °C, the transmission strongly decreases due to a partial surface reduction of the oxide that gives rise to electronic absorption,[29] but it is still possible to recognize the signal of 2,6-DMP at the maximum pressure (Fig. 3b, solid line). In addition to physisorbed 2,6-DMP signals, the band located at 1613 cm^{-1} is still evident (related to the presence of L sites), and the lack of the bands related to 2,6-$DMPH^+$ (B species) suggests the absence (or a minimal) of B acidity. No signals were observed after evacuation (Fig. 3b, short dash line), but this can also be due to the low transmittivity of the sample.

Tungsten oxide WO_3 is considered a very acidic transition metal oxide. Many studies confirmed the presence of B acidity when WO_3 is supported on different metal oxides (such as

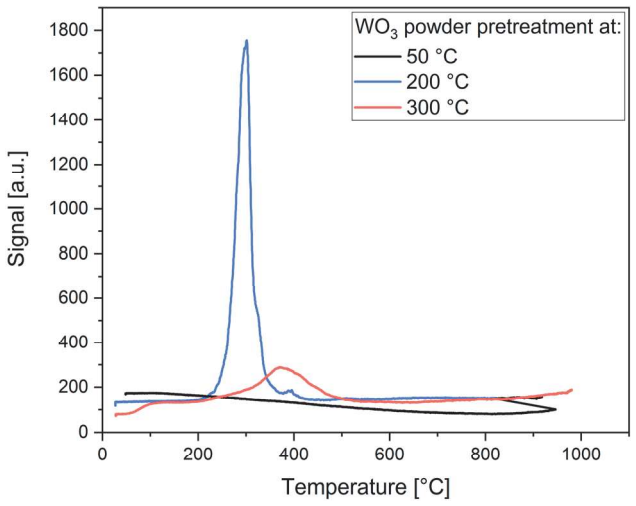


Fig. 2 NH_3 TPD profiles carried out on the WO_3 sample activated at 50, 200, and 300 °C.

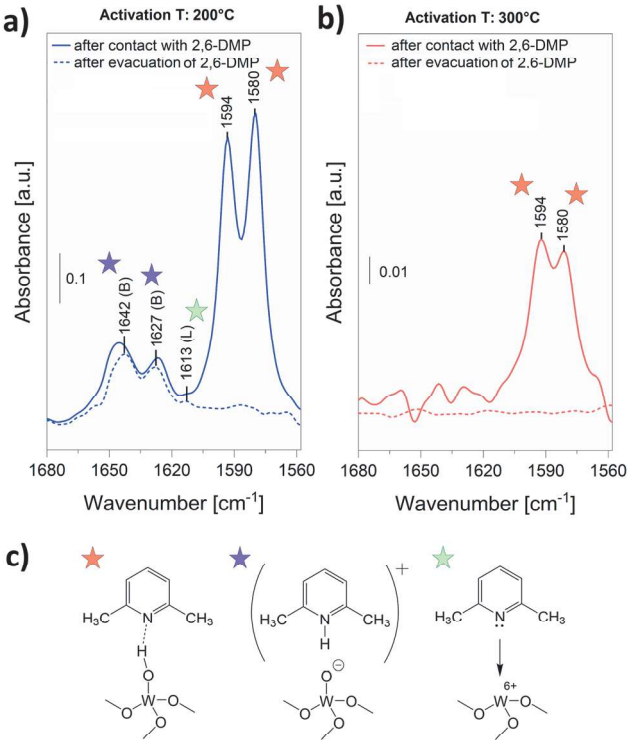


Fig. 3 Differential absorbance spectra relative to the adsorption/desorption of 2,6-DMP on the WO_3 sample, activated at (a) 200 and (b) 300 °C, after contact at RT with the vapor pressure of 2,6-DMP (solid lines) and after RT evacuation of 2,6-DMP excess (short dash lines). (c) Representation of H-bonded and physisorbed 2,6-DMP molecules (orange star), 2,6-$DMPH^+$ held to the surface, indicating the presence of Brønsted (B) acid sites (purple star), and 2,6-DMP molecules interacting with coordinatively unsaturated W^{6+} cations (green star).

This journal is © The Royal Society of Chemistry 2026

silica, alumina, and zirconia), but only very few studies have been devoted to the acid properties of unsupported tungsten oxides.[30] The presence of both B and L sites on the m-WO_3 surface for the sample activated at 200 °C is consistent with the literature studies on m-WO_3 evacuated at RT and activated at 100 °C. Surface coordinatively unsaturated W^{6+} ions are responsible for L acidity, while B acidity has been correlated to the presence of surface W–OH groups. The modification of the surface acidic properties, when the sample is activated at a higher temperature (and in the present case at 300 °C), may be related to surface reconstruction processes.

2.3 *Operando* DRIFTS characterization under N_2 and dry synthetic air

Operando DRIFT spectroscopy on the WO_3-based sensor kept under a continuous 100 sccm flux of N_2 or dry synthetic air was performed to deeply investigate the influence of the operating temperature on both sensing film electrical properties and surface chemistry. In both Fig. 4a and 5a, the single channel $I_{background}$ was recorded after the sensor resistance was stabilized at a working temperature of 50 °C, while the single channel $I_{samples}$ were acquired during the periods of time evidenced in the resistance *vs.* the time graph by the blue and red bars, respectively. eqn (1) described in section 5.4 "DRIFT Spectroscopy and Electrical Characterization Setup" was used to obtain the absorbance (AB) spectra named SCAN 200 °C and SCAN 300 °C in Fig. 4b and 5b.

Fig. 4a shows the variation of the film resistance by increasing steps of operating temperature from 50 °C to 200 °C and 300 °C, while the sensor was exposed to a N_2 atmosphere. The resistance of the film decreased from 6.7 MΩ at 50 °C to 8.5 kΩ at 200 °C, and further to 2.8 kΩ at 300 °C. This behaviour is attributed to the thermal excitation of electrons from donor levels to the conduction band (CB), which resulted in an increased concentration of negative charge carriers (e^-), thereby leading to a decrease in electrical resistance. Fig. 4b displays the absorbance (AB) spectra acquired at sensor working temperatures of 200 °C and 300 °C. The AB spectrum SCAN 200 °C shows several downward peaks across a wide range of wavenumbers, indicating that the increase in temperature resulted in a decrease in surface chemical species, namely physisorbed water molecules (1644 and 1620 cm^{-1} [31–33]) and W–O bonds (2060, 1865, 1425, 1043, and 872 cm^{-1} [32,34–36]). The AB spectrum at 300 °C reveals that most of these deficiencies persisted, although the upward peak at 975 cm^{-1} highlighted the increase of new bonds. The attribution of this peak is postponed in the section 3 "Discussion", as the literature presents challenges in identifying a definitive assignment.

Fig. 5a depicts the variation of the film resistance under the same incremental steps of operating temperature applied in

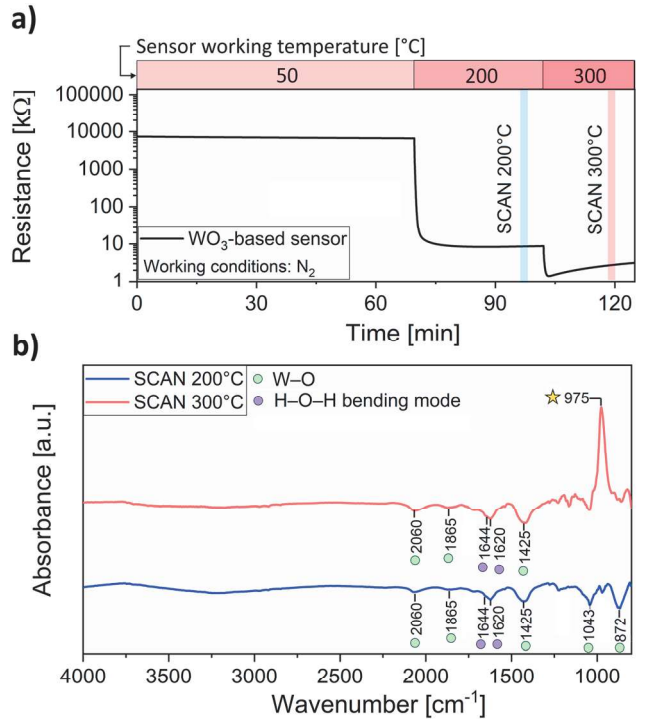


Fig. 4 (a) Sensor resistance in the N_2 atmosphere at working temperatures of 50, 200 and 300 °C. (b) DRIFT AB spectra with background subtraction and signal processing acquired on the WO_3 sensing layer during SCAN 200 °C and SCAN 300 °C, represented in (a). Circular labels denote clear peak assignments, while the yellow star indicates one that requires discussion. The temperature and relative humidity inside the test chamber during the tests were ~30 °C and ~1% RH, respectively.

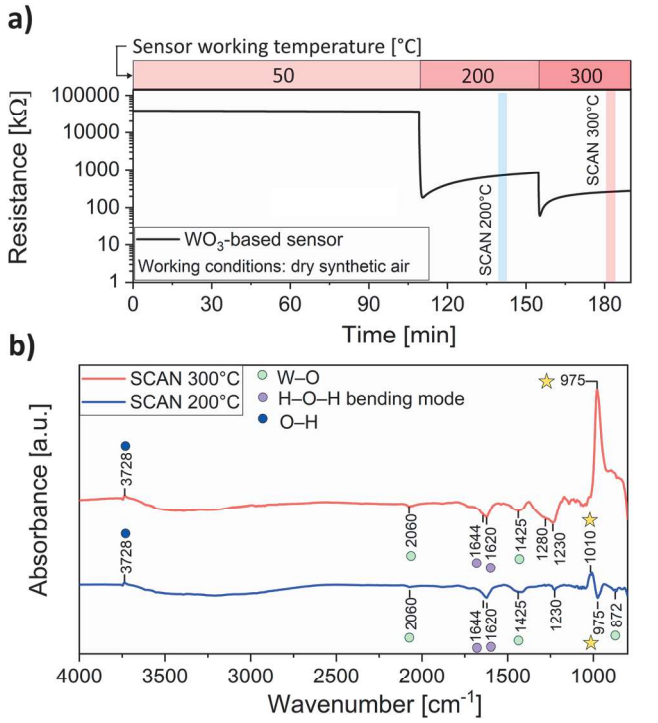


Fig. 5 (a) Sensor resistance in dry synthetic air at working temperatures of 50, 200 and 300 °C. (b) DRIFT AB spectra with background subtraction and signal processing acquired on the WO_3 sensing layer during SCAN 200 °C and SCAN 300 °C, represented in (a). Circular labels denote clear peak assignments, while the yellow stars indicate those requiring discussion. The temperature and relative humidity inside the test chamber during the tests were ~30 °C and ~1.5% RH, respectively.

Fig. 4a, but in dry air. The resistance of the film decreased from 35 MΩ at 50 °C to 0.79 MΩ at 200 °C, and further to 0.28 MΩ at 300 °C. When comparing the values at corresponding operating temperatures, the resistance in dry air was consistently higher than that in N_2. This observation can be attributed to the well-documented phenomenon of O_2 ionosorption, which reduces the number of majority carriers and increases the Schottky barrier height between the nanostructures composing the sensing film.[37–39] Fig. 5b displays the AB spectra acquired at sensor working temperatures of 200 °C and 300 °C, emphasizing several similarities with those collected for N_2, particularly in the position and intensity of the peaks within the 2100–800 cm^{-1} range. An exception is the upward peak at 1010 cm^{-1} observed in the SCAN 200 °C, which is tentatively assigned to the formation of superoxo species (O_2^-). These species are typically formed at low activation temperatures on the surface of metal oxides as a result of O_2 ionosorption, and are subsequently converted into O^- at higher temperatures.[40,41] A peak at a similar wavenumber (1050 cm^{-1}) was previously reported for WO_3 by Junker *et al.*,[42] who discussed the scarcity of literature assignments and suggested the O_2^- origin based on FTIR studies of other materials. Another visible difference in Fig. 5b compared to Fig. 4b is the rise of a peak at 3728 cm^{-1} for the spectra at both temperatures, attributed to the formation of terminal hydroxyl groups.[31] These groups are formed due to a low content of H_2O in the dry air stream.

2.4 *Operando* DRIFTS characterization with target molecules

Operando DRIFTS was carried out on the WO_3 sensor operated at 200 °C and 300 °C in the presence of 0.5, 1, 2, 4, and 8 ppm of D-limonene in the carrier of dry air, to explore the mechanism governing the device sensitivity. The single channel $I_{background}$ was acquired after the sensor resistance stabilized in dry air at the working temperature used for the investigation, while the single channels $I_{samples}$ were recorded during the periods of time evidenced in Fig. 6(a), (c) and (d) by the colored bars. Eqn (1) described in section 5.4 ''DRIFT Spectroscopy and Electrical Characterization Setup'' was used to obtain the AB spectra named SCANs 1–5 in Fig. 6(b), (d) and (f).

The WO_3 film resistance decreased under exposure to D-limonene (see Fig. 6), leading to the sensor response in the carrier of dry air shown in Fig. S4. The best working temperature was 200 °C, as previously demonstrated with a different testing set-up.[25] The sensor response and recovery times at 200 °C and 300 °C, calculated as described in section 5.4, are summarized in Table S1. A shorter $t_{90_response}$ was observed at 300 °C, whereas a shorter $t_{10_recovery}$ was achieved at 200 °C. Response and recovery kinetics on the order of minutes have been previously observed for thick-film gas sensors.[25]

DRIFT spectra during exposure to the analyte at 200 °C and 300 °C presented up- and down-ward peaks that intensified as the D-limonene concentration increased from 0.5 to 8 ppm (Fig. 6). The integrated peak intensities of the most significant signals are summarized in Table S2, while the peak fitting of SCAN 5 (8 ppm) at 200 °C and 300 °C is presented in Fig. S5 as a representative example. Fig. 7 shows the evolution of the integrated peak intensities as a function of the analyte concentration, whereas Fig. S6 and S7 report the correlation between the response change and the absolute integrated intensities of selected spectral bands.

**Both the AB spectra in Fig. 6b and d show downward peaks at 2060, 1865, and 1430 cm^{-1}, whose intensities exhibit a similar trend as a function of analyte concentration (Fig. 7a and b). These bands are characteristic of a reduction in W–O bonds.[32,34–36] Peaks in the region of hydroxyl groups (3800–3000 cm^{-1}) indicated that these species were also interacting with D-limonene. The spectra under both temperature conditions evidenced a decrease in terminal –OH groups (downward peaks at 3741 and 3730 cm^{-1}); meanwhile, *n*-fold coordinated –OH increased at 200 °C, Fig. 6b (positive peaks at 3680 and 3610 cm^{-1}) and decreased at 300 °C, as shown in Fig. 6d (a negative peak at 3635 cm^{-1}). At a working temperature of 200 °C, the integrated intensities of the negative bands assigned to terminal –OH groups and the positive bands assigned to bridging –OH groups showed similar dependence on the D-limonene concentration (Fig. 7c). The concurrent decrease of terminal hydroxyl species and increase of bridging hydroxyl species suggest that these two surface species are correlated during D-limonene detection, with the formation of bridging –OH groups occurring alongside the consumption of terminal –OH groups. In contrast, at 300 °C, the absolute intensities of the negative terminal and bridging –OH bands did not exhibit the same gas concentration dependence. In particular, the decrease in the bridging –OH band is more pronounced than that of the terminal –OH bands as the limonene concentration increases (Fig. 7d), suggesting that the two hydroxyl species do not evolve in a directly correlated manner during limonene exposure. The bands centered at 3400 and 3200 cm^{-1} reflect changes in interacting –OH groups, increasing at 200 °C and decreasing at 300 °C. A major difference between SCANs acquired at 200 °C and 300 °C lies in the upward peaks at the lowest wavenumbers, which was centered at 985 cm^{-1} in the first case and at 1030 cm^{-1} in the second case. As shown in Fig. 7a and b, the intensity of both peaks increased with increasing analyte concentration. At low D-limonene concentrations, the peak at 985 cm^{-1} was not sufficiently resolved from the noise to allow reliable integration. As these peaks require a more thorough interpretation, they will be addressed in section 3 ''Discussion''.

Fig. S6 and S7 show a generally increasing correlation between the sensor response and the absolute integrated intensity of the specific IR bands listed in Table S2 and discussed above. This behaviour indicates that the surface species associated with these bands are involved in the limonene sensing mechanism, as their evolution follows the increasing trend of the sensor response. The only exception is the band at 3200 cm^{-1} at an operating temperature of 300 °C, whose integrated intensity exhibits a non-monotonic trend that did not correlate with the electrical response, suggesting that the corresponding surface species (interacting –OH) did not play a major role in the sensing process under these conditions.

This journal is © The Royal Society of Chemistry 2026

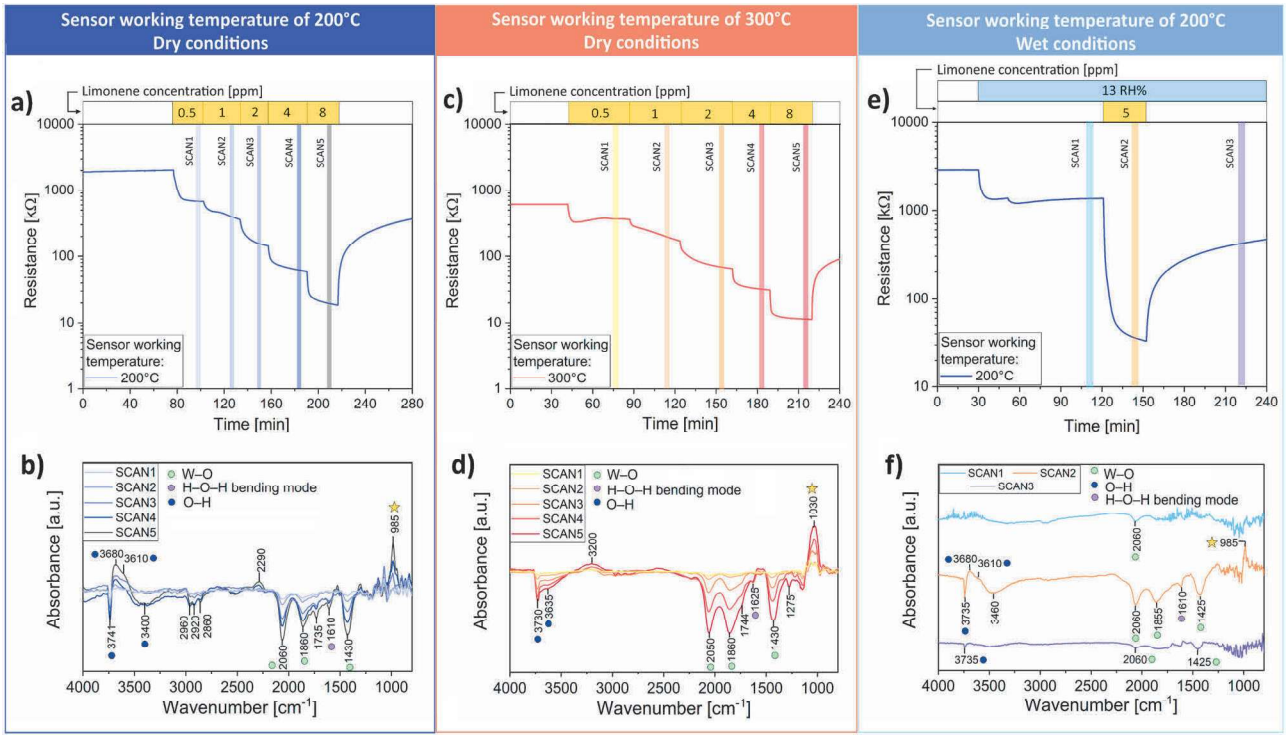


Fig. 6 Electrical resistance of the WO_3 sensor operated at (a) 200 °C and (c) 300 °C to 0.5, 1, 2, 4, and 8 ppm of D-limonene. (b) and (d) DRIFT AB spectra with background subtraction and signal processing acquired on the WO_3 sensing layer during SCANs 1–5, represented in (a) and (c). The temperature and relative humidity inside the test chamber during the tests in (a) and (c) were ~30 °C and ~1.5% RH, respectively. (e) Electrical resistance of the WO_3 sensor operated at 200 °C to 5 ppm of D-limonene in the presence of 13% RH (the temperature inside the chamber is equal to ~30 °C). (f) DRIFT AB spectra with background subtraction and signal processing acquired on the WO_3 sensing layer during SCANs 1–3, represented in (e). Circular labels denote clear peak assignments, while the yellow stars indicate those requiring discussion.

Negative peaks at 2960, 2920, and 2860 cm^{-1}, corresponding to CH stretching vibration,[43] along with signals at 1735 and 1744 cm^{-1}, indicative of C=O,[44] suggest the release of residual surface carbon species.

DRIFT spectra recorded during sensor recovery periods (Fig. S8a and b) indicated that the WO_3 surface was not fully regenerated at either 200 and 300 °C within the duration of the experiment, as the oxygen- and hydroxyl-related surface species were not completely restored after being consumed during the reaction with D-limonene, consistent with the electrical measurements. Moreover, the positive band at 985 cm^{-1} disappeared, whereas that at 1030 cm^{-1} decreased in intensity, indicating that these spectral changes induced by D-limonene exposure were reversible.

Under the best operating condition, namely at a working temperature of 200 °C, the sensor was also exposed to 13% RH at 30 °C, followed by addition of 5 ppm of D-limonene. Transitioning from dry to wet conditions, the film resistance decreases by approximately 2 MΩ (Fig. 6e), while SCAN1 primarily indicates a reduction in W–O bonds (a downward peak at 2060 cm^{-1}, Fig. 6f). The absence of peaks corresponding to a noticeable increase in the number of hydroxyl groups suggests that, even under dry conditions, the surface had already almost reached equilibrium for this species and that such equilibrium is not influenced by modest rises in humidity. Addition of D-limonene further decreased the sensor resistance leading to a response of 39, which is slightly lower than the value expected from the calibration curve under dry conditions (Fig. S4). H_2O is a well-known interfering agent, typically strongly reducing the sensor responses to the target gases by changing the surface chemistry (*e.g.*, through hydroxylation), leading to a decreased reactivity, or by covering the active sites *via* steric hindrance, preventing them from interacting with the analyte.[5,6] The invariance of the sensor response to the level recorded under dry conditions was a non-negligible result. Comparing SCANs in Fig. 6b with SCAN 2 in Fig. 6f, the similarities in both the position and the intensity of the AB peaks are evident, indicating that the sensing mechanism is not influenced by humidity. The decrease in response can therefore be mainly attributed to the steric hindrance effect of H_2O layers, which only partially limits the interaction between the active sites and the analyte.

The surface reactivity of the sensor at a working temperature of 200 °C was further evaluated through *operando* DRIFTS using NO_2 as the probe molecule under dry conditions. Exposure to 3 ppm NO_2 induced a marked increase in sensor resistance (Fig. S9a), accompanied by the formation of surface hydroxyls, W–O bonds, and chemisorbed NO_2 species (monodentate nitrites and nitro compounds).[45] The latter are associated with coordinatively unsaturated metal cations (Fig. S9b).[46]

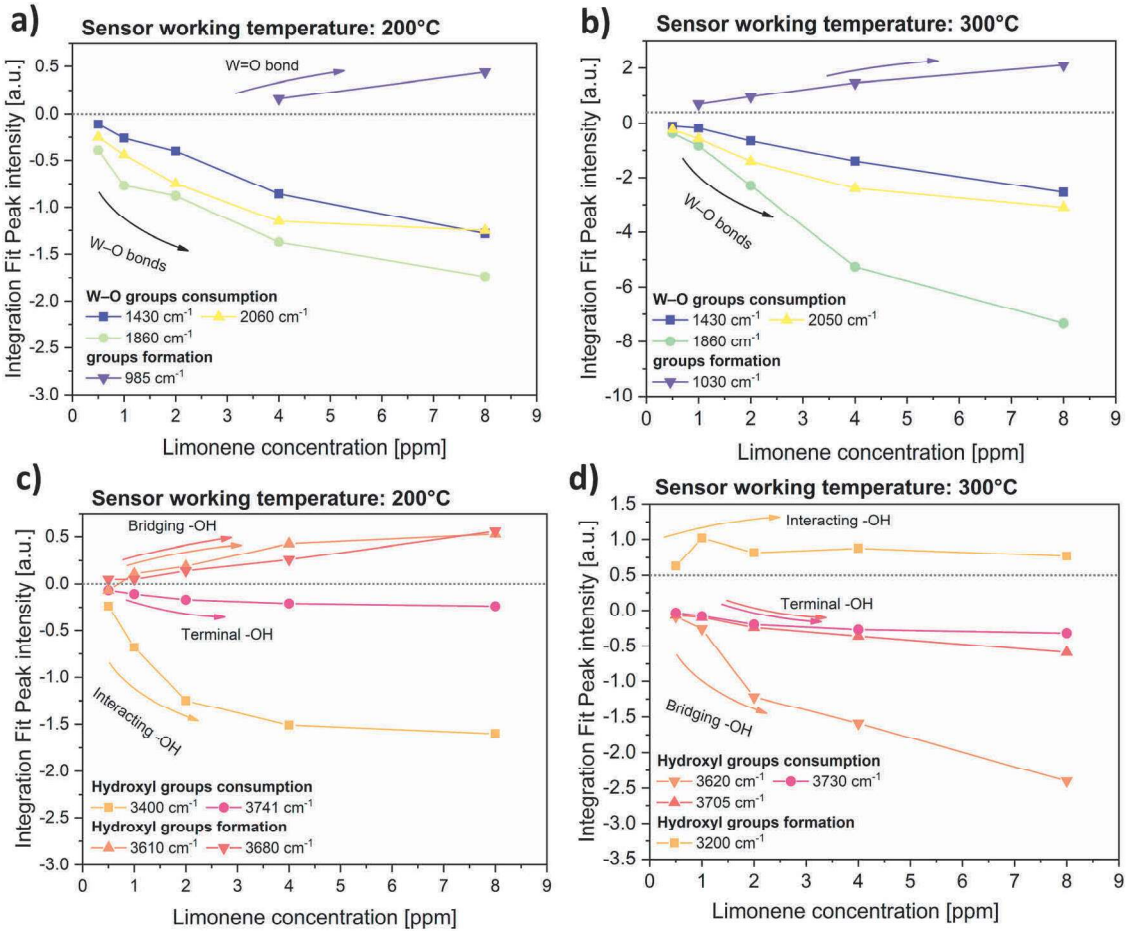


Fig. 7 Evolution of the integrated peak intensity as a function of analyte concentration. Panels (a) and (b) show the analysis of peaks in the 2100–800 cm^{-1} spectral range at working temperatures of 200 and 300 °C, respectively. Panels (c) and (d) show the analysis of peaks in the 4000–2900 cm^{-1} spectral range at working temperatures of 200 and 300 °C, respectively.

To further investigate the origin of sensor selectivity, *operando* DRIFTS measurements were also performed during acetone exposure (Fig. S10). Although acetone elicited only a limited sensor response at both operating temperatures of 200 °C and 300 °C, consistent with previous electrical measurements.[25] The spectra indicate the consumption of W–O surface species. At 200 °C, a positive band at 980 cm^{-1} was observed, as also found during D-limonene exposure. Instead, surface hydroxyl groups were not involved.

3. Discussion

3.1 Origin of the superior D-limonene sensing performance of WO_3: the role of surface Lewis acidity

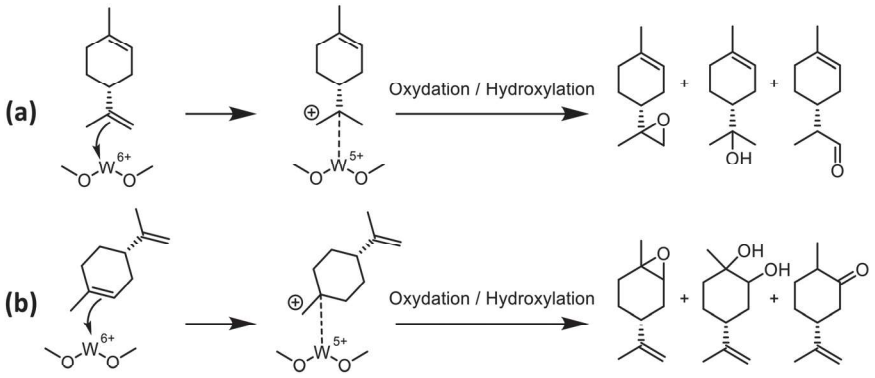
The superior D-limonene sensing performance of nanoflaked WO_3 originates from its pronounced surface Lewis acidity. While previous studies reported enhanced responses of WO_3 compared to SnO_2 and ZnO for D-limonene detection,[25] the intrinsic physicochemical origin of this behaviour had not been clarified in mechanistic terms.

TPD of 2,6-DMP and DRIFTS with NO_2 as the probe molecule confirmed the presence of surface coordinatively unsaturated W^{6+} ions when the material was activated at 200 °C, namely the best working temperature for D-limonene sensing. These sites constitute strong Lewis's acid centers capable of efficiently activating C=C double bonds.

Among transition-metal oxides, WO_3 is recognized as one of the most acidic materials. The stronger Lewis acidity of W^{6+} compared to Zn^{2+} or Sn^{4+} provides a rational explanation for the enhanced interaction with unsaturated hydrocarbons.[4] In this context, D-limonene oxidation likely proceeds *via* the formation of carbocation intermediates (Scheme 1(a) and (b)), followed by successive reactions with lattice oxygen species or surface hydroxyl groups. Similar carbocation-mediated activation pathways on WO_3 have been reported in alkene oxidation catalysis.[47–49] The ability of W^{6+} to efficiently polarize and activate π-bonds thus emerges as a key microscale descriptor governing sensing performance.

From a design perspective, these findings suggest that next-generation alkene sensors should be engineered by deliberately increasing both the density and intrinsic strength of surface Lewis acid sites. This may be achieved through doping with high-valent, small-radius cations, such as V^{5+}, Mo^{6+}, Zr^{4+}, Nb^{5+}, Ta^{5+}, Ti^{4+}, and Al^{3+}.[50–52] In addition to lattice substitution,

 This journal is © The Royal Society of Chemistry 2026



Scheme 1 Carbocation intermediate formation on D-limonene (a) isopropenyl group and (b) cyclic double bond, and possible products of the reaction.

these elements may also function as promoters when introduced as highly dispersed surface clusters or isolated species, by creating new strong Lewis acid sites without significantly perturbing the bulk structure of the host oxide.[52–55] Beyond compositional tuning, low-coordinated cations exposed at surface topological structural defects, such as steps, kinks, corners, and dislocations, represent powerful levers for modulating Lewis acidity.[4,56] Consequently, defective regions typically display markedly higher Lewis acidity than flat, well-ordered terrace surfaces, where metal cations are fully coordinated and less reactive. In this respect, it is noteworthy that the WO_3 employed in the present study exhibits a nanoflake morphology characterized by surface imperfections, which likely promotes the preferential exposure and stabilization of coordinatively unsaturated W^{6+} species.

These considerations demonstrate how microscale chemical descriptors can guide rational material design, in direct alignment with the multiscale objective outlined in the Introduction section.

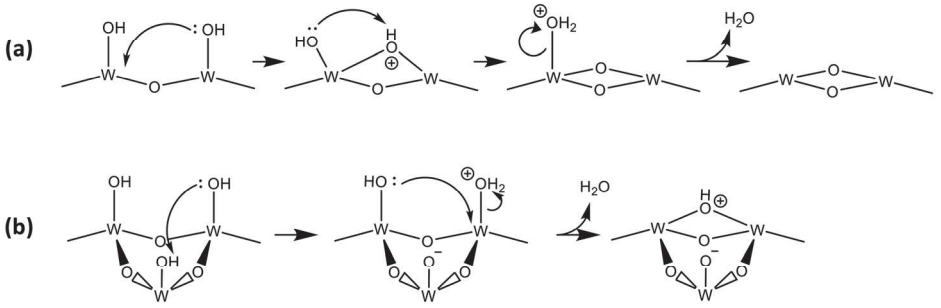
3.2 Temperature-induced surface reconstruction

Dynamic chemisorption, differential absorbance spectra relative to the adsorption/desorption of 2,6-DMP, and *operando* DRIFT measurements acquired on the WO_3 sensor activated at 200 °C and 300 °C highlight a surface reconstruction induced by temperature, which impacted the sensing capabilities *vs.* D-limonene.

Dynamic chemisorption measurements show that increasing the temperature from 200 °C to 300 °C profoundly changes the NH_3 TPD profiles of the WO_3 sample, strongly reducing the number of acidic sites while increasing their strength.

The high sensor response observed at 200 °C suggests that the acidic sites present at this temperature participate as active sites for gas detection. From differential absorbance spectra relative to the adsorption/desorption of 2,6-DMP, the acidity of the sample activated at 200 °C is attributed to both stable Brønsted and Lewis sites on the m-WO_3 surface, namely W–OH groups and coordinatively unsaturated W^{6+} ions, respectively. The reactivity of these sites toward various gases has been confirmed in previous studies,[4,44,57] and the critical role of coordinatively unsaturated W^{6+} ions has been discussed above in detail.

The decrease in the overall number of acidic sites on WO_3 at 300 °C, as evidenced by dynamic chemisorption, may explain the reduced sensor response at this temperature. According to Kanan *et al.*,[35] exposing m-WO_3 to a temperature increase from 200 °C to 300 °C led to a condensation of adjacent surface W–OH groups, as depicted in Scheme 2(a), leading to the formation of bridged oxygens. Although not acidic, W–O–W sites may still participate in reactions with D-limonene, with different reactivity. Indeed, the sensor response remains relatively high even at low D-limonene concentrations, implying that the surface is still rich in active sites. Moreover, the newly emerging low intense peak centered at 370 °C in the NH_3 TPD profile suggests the presence of different acid sites. An accurate definition of the nature of these strongly acidic sites based on the FTIR spectra with 2,6-DMP is hindered by the low



Scheme 2 Mechanism of adjacent surface W–OH group condensation leading to (a) W–O–W and (b) $-OH^+$ sites.

transmittance of the sample. Based on the condensation of adjacent hydroxyl groups, we hypothesize that the reaction shown in Scheme 2(b) may occur, leading to the formation of strongly acidic bridging –OH^+ sites.

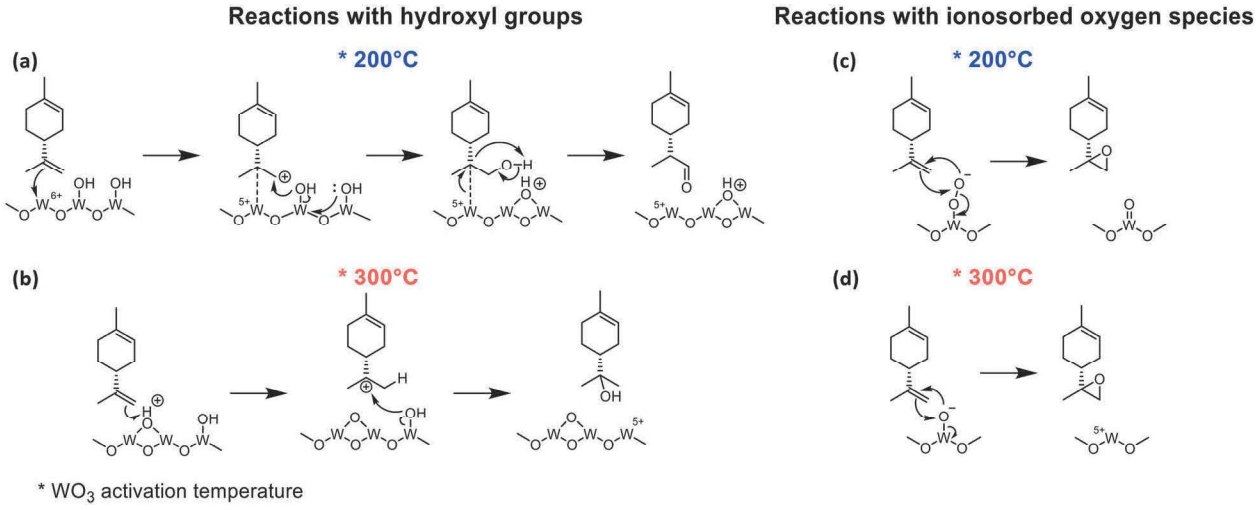
In addition, Kanan *et al.*[35] demonstrated by XPS that WO_3 samples evacuated at room temperature exhibited mainly W^{6+} species, whereas additional contributions assigned to W^{5+} and W^{4+} appeared after evacuation at 150 and 400 °C, indicating that temperature can promote the formation of reduced tungsten species. These changes were correlated with a decrease in the Lewis acidity of the surface, as determined from pyridine adsorption experiments. Although *in situ* XPS measurements were not performed in the present study, the electrical characterization of the WO_3 film, together with the appearance of negative IR bands associated with consumption of W–O, provides indirect evidence of partial surface reduction upon heating. Such a reduction may contribute to the decrease in surface acidity observed by NH_3-TPD, through modifications of the electronic structure and coordination environment of surface tungsten sites. The lower Lewis acidity of coordinatively unsaturated W^{5+} compared to W^{6+} may reduce their ability to activate the C=C bonds of D-limonene during the intermediate steps of the gas-phase reaction.

Although dynamic chemisorption and differential absorbance spectra related to the adsorption/desorption of 2,6-DMP are fundamental for studying the acidic properties of the surface, DRIFT spectra of the sensing film activated at 200 °C and 300 °C in N_2 and dry air aim to provide a broader identification of surface site variations, including oxygen species, which are usually highly reactive with reducing gases like D-limonene. At both temperatures, a decrease in W–O bond content and physisorbed H_2O was observed. The main difference in the AB spectrum acquired at 300 °C compared to that at 200 °C lies in the peak at 975 cm^{-1}, which indicates the formation of new sites at the higher temperature. In the literature, the band has been ascribed to the W=O stretching vibration mode of terminal oxygen.[32,58–61] The AB spectra in Fig. 4b and 5b exhibit similar patterns, despite being acquired under different atmosphere (N_2 and dry air, respectively), suggesting minimal contribution from external O_2 interactions. Therefore, the origin of the W=O sites can be primarily associated with modifications in the local coordination environment of surface tungsten sites. Previous studies have shown that WO_3 samples characterized by structural disorder and oxygen-deficient tungsten oxide structures exhibit Raman and IR bands at around 940 and 970 cm^{-1}, respectively, assigned to terminal W=O species,[60,61] highlighting the sensitivity of these species to local oxygen rearrangement. Accordingly, the emergence of the 975 cm^{-1} band upon heating may indicate the formation of additional locally modified WO_{3-x}-like surface environments at 300 °C.

3.3 Temperature-dependent divergence of reaction pathways in D-limonene sensing

Operando DRIFTS revealed that D-limonene detection on WO_3 did not proceed through a single invariant mechanism; rather, the operative reaction pathway diverges as a function of temperature, reflecting the underlying reconstruction of surface acidity, oxidation state, and oxygen speciation discussed above. The distinct sensing responses observed at 200 °C and 300 °C therefore arise from chemically differentiated surface regimes. The following hypotheses are proposed based on the interpretation of the data, although they are not intended to provide exhaustive explanations, as the complexity of the system would recognize that multiple mechanisms may coexist simultaneously.

At a sensor operating temperature of 200 °C, Scheme 3(a) first represents the D-limonene carbocation intermediate evolution for interaction with a W^{6+} site. Then, it provides a mechanistic interpretation for the decrease in terminal hydroxyl groups, which results in the formation of bridged –OH, as evidenced by the AB spectra of WO_3 activated at 200 °C (Fig. 6b). On the other hand, at 300 °C (Fig. 6d), both terminal and bridged –OH are consumed, supporting Scheme 3(b), which



Scheme 3 D-Limonene reaction mechanism with WO_3 surface sites at operating temperatures of 200 °C and 300 °C involving (a) coordinatively unsaturated W^{6+} and terminal W–OH groups, (b) bridged –OH^+ sites and terminal W–OH groups, (c) superoxide ion (O_2^-.), and (d) oxygen anion (O^-.).

This journal is © The Royal Society of Chemistry 2026

involves the participation of strong acidic –OH^+ sites formed as described in Scheme 2(b). Scheme 3(c) and (d) depict pathways of surface reduction induced by the reaction of D-limonene with oxygen ions, which have been identified in the literature as the principal sites formed *via* O_2 ionosorption at 200 °C (O_2^-) and 300 °C (O^-).[40,41] In particular, the reaction in Scheme 3(c) would explain the rise of the peak observed in Fig. 6b at 985 cm^{-1}, attributed to W═O.[31–33,58,59,62] The same peak was not detected in the AB spectra acquired at 300 °C (Fig. 6d), where instead the growth of the peak at 1030 cm^{-1} was recorded, whose interpretation is not straightforward. A band at a similar wavenumber was recently reported in an *operando* DRIFTS study of a photoactivated WO_3 sensor, where the authors hypothesized that it could be associated with ionized oxygen species, while acknowledging that no definitive assignment was available in the literature.[42] In our case, however, the positive correlation between the intensity of the 1030 cm^{-1} band, the limonene concentration (Fig. 7b), and the sensor response (Fig. S7) makes this interpretation unlikely, as exposure to a reducing gas such as limonene is expected to consume ionized oxygen species rather than promote their accumulation on the sensor surface. Previous studies have assigned bands in the 1020–1080 cm^{-1} region on tungsten-based materials to W–C stretching, C–O stretching, and C–C vibrational modes.[44,63–65] Therefore, the emergence of the 1030 cm^{-1} band in our spectra may be related to the formation of a surface reaction intermediate, although additional evidence is required to support this hypothesis.

At an operating temperature of 200 °C, as exposed to 13% RH at 30 °C, SCAN 2 in Fig. 6f, acquired during sensor interaction with D-limonene, exhibits AB peaks with both the position and the intensity closely matching those observed in the SCANs reported in Fig. 6b, which were collected under dry conditions. This strong similarity suggests that the sensing mechanisms proposed in Scheme 3(a) and (c) remain operative also under these mildly humid conditions.

Operando DRIFTS measurements performed under acetone exposure revealed the consumption of W–O surface species, whereas no significant involvement of surface hydroxyl groups or reaction intermediates was observed. Although acetone produced only a limited sensor response, it was previously identified as a strong interferent in cross-selectivity measurements.[25] This behaviour can be rationalized considering that acetone preferentially adsorbs through the oxygen atom of its carbonyl group onto under-coordinated W surface cations, as derived from density functional theory (DFT) calculations.[66] Moreover, similar to D-limonene, acetone also induces the growth of the IR band at 980 cm^{-1}, suggesting that both analytes follow a common reaction pathway involving the consumption of superoxide species and the formation of W═O surface groups. Consequently, the marked decrease in the limonene response observed in the presence of acetone is likely due to the competition between the two analytes for both the same active W surface sites and reactive superoxide species, thereby reducing the availability of the surface species required for limonene activation and oxidation.

3.4 Comparative analysis, innovative aspects, and research outlook

Vibrational spectroscopic techniques have previously been used to investigate the gas-sensing mechanisms of MOXs towards small molecules and simple VOCs employing both *in situ* and *operando* approaches.[6,7,42,44,57,67–69] While *in situ* spectroscopic techniques provide an indirect observation of the sensing process by characterizing the sensing material, *operando* approaches enable the direct observation of the active sensing layer under realistic operating conditions, accounting for the effects of film deposition, device architecture, and film–gas interaction kinetics on sensing performance. Accordingly, the methodology proposed in this work employs *operando* DRIFTS to directly investigate the functional properties of the sensing layer in the actual sensing device.

For WO_3-based gas sensors, *operando* DRIFTS has been employed to assess the influence of WO_3 morphology on the sensing mechanisms of NO_2 and CO,[57] and, more recently, to elucidate the sensing mechanisms of common VOCs such as ethanol, toluene, acetone, and acetylene in combination with catalytic combustion measurements.[44] The latter study demonstrated that the widely accepted combustion model based on the complete oxidation of VOCs to CO_2 *via* chemisorbed oxygen must be reconsidered.[44] However, without a prior characterization of the surface-site landscape, *in situ* and *operando* vibrational spectroscopies often lack the chemical specificity required to identify all active sites governing sensing performance. Consequently, establishing predictive structure–property relationships for WO_3-based gas sensors operating under different conditions (*e.g.*, working temperature) remains challenging.

The present case study highlights this limitation. Although *operando* measurements clearly revealed temperature-dependent changes in both the limonene response and reaction pathways, the microscopic origin of these differences would have remained elusive without the complementary characterization of the acid sites and their temperature-dependent evolution by means of NH_3-TPD and FT-IR using 2,6-DMP as a probe molecule.

Moreover, to the best of our knowledge, this work provides the first experimental framework for rational improvement of alkene sensing by tuning the surface Lewis acidity through coordinatively unsaturated high-valent metal cations.

Beyond the specific WO_3/D-limonene case study, the proposed methodology offers a general blueprint for establishing mechanistic correlations between the microscopic surface chemistry and the macroscopic sensing performance of gas sensors. The same strategy can be extended to emerging sensing materials, including heterojunction metal oxides,[70] plasmonic- or catalyst-modified oxides,[71,72] 2D materials[73,74] and photoactivated sensing platforms, where identifying the active surface sites remains essential for rational materials design.

4. Conclusions

This work demonstrates that an integrated, *operando*-oriented multi-characterization strategy enables a multiscale understanding

of chemoresistive sensing by providing causal links between microscale surface chemistry and macroscale device performance. By combining temperature-dependent sensor electrical characterization with NH_3-TPD, FT-IR spectroscopy using the 2,6-DMP probe molecule, and *operando* DRIFTS performed on the working sensor, we establish structure–property–function relationships governing the sensing behaviour of nanostructured WO_3 under realistic operating conditions. This approach transforms chemoresistive sensing from a largely phenomenological description into a mechanism-resolved functional paradigm.

At the microscale, we reveal that the surface chemical functionality of WO_3 is strongly temperature-dependent and plays a decisive role in D-limonene detection. At 200 °C, NH_3-TPD and FT-IR analyses with 2,6-DMP identify medium-strength Lewis acidic sites associated with coordinatively unsaturated W^{6+} centers. These sites are proposed to activate the C=C double bonds of D-limonene more effectively than the corresponding cations in SnO_2 or ZnO, rationalizing the superior sensing performance of WO_3. *Operando* DRIFTS further shows that terminal hydroxyl groups participate directly in the sensing mechanism, leading to their consumption and the formation of *n*-fold coordinated –OH species. The emergence of a band at 985 cm^{-1}, increasing with analyte concentration, indicates the formation of new W=O bonds, likely arising from reactions with superoxide ions. Importantly, moderate humidity does not alter this mechanism, underscoring the robustness of the surface chemistry at this operating temperature.

At 300 °C, the microscale surface landscape undergoes a marked transformation. NH_3-TPD evidences a reduction in the total number of acidic sites accompanied by an increase in their strength of acidic sites, suggesting a temperature-induced surface reconstruction. Although the low surface coverage and reduced optical transmittance hinder a definitive spectroscopic assignment, *operando* DRIFTS reveals a qualitatively different reaction pathway. We hypothesize that the condensation of adjacent hydroxyl groups may lead to the formation of strongly acidic bridged $–OH^+$ sites, which could act as active centers in D-limonene detection at higher sensor working temperatures. This reaction pathway would explain the consumption of *n*-fold coordinated –OH groups, together with the terminal ones, as observed in the AB spectra acquired in *operando* DRIFT spectroscopy. The disappearance of the 985 cm^{-1} band and the progressive growth of a feature at 1030 cm^{-1} point to a distinct sensing mechanism at 300 °C, likely involving different surface reaction pathways or reaction intermediates. Although the origin of the 1030 cm^{-1} band remains uncertain, its evolution with increasing limonene concentration highlights its close association with the sensing process. Further investigations are required to elucidate the nature of the surface species responsible for this feature.

Operando DRIFTS measurements identified a common reaction pathway f acetone and D-limonene, involving the formation of W=O groups. Competitive adsorption over under-coordinated W surface cations and competition for reactive oxygen species were identified as a mechanistic insight into the observed interferent role of acetone.

Beyond elucidating the sensing mechanism of WO_3 toward D-limonene, this study identifies surface Lewis acidity as a key functional descriptor for alkene detection. The results suggest that deliberate engineering of coordinatively unsaturated high-valent cations represents a promising strategy for next-generation MOX-based sensors. More broadly, the presented methodology offers a general blueprint for transforming gas sensing from empirically optimized systems into predictively designed functional materials, fully consistent with the multiscale paradigm underpinning advanced gas-sensing technologies.

5. Experimental section/methods

Fig. 8 summarizes the integrated experimental strategy adopted to elucidate the sensing mechanism. Temperature-dependent electrical characterization provides the macroscale readout, identifying characteristic operating regimes of the device. At the microscale, temperature-programmed desorption and FT-IR spectroscopy with adsorbed 2,6-dimethylpyridine determine the density, strength, and nature (Brønsted/Lewis) of surface acid–base sites as a function of thermal treatment. Finally, *operando* DRIFTS measurements performed under working conditions bridge these length scales by directly correlating the evolution of surface species with the simultaneous resistance response, enabling the identification of the active sites governing the temperature-dependent sensing behaviour.

5.1 Materials synthesis

All materials were used as received without further purification. Tungstic acid (H_2WO_4) and oxalic acid dihydrate ($H_2C_2O_4 \cdot 2H_2O$) were purchased from Alfa Aesar (Haverhill, MA, USA) (purity 99.5–102.5%), acetonitrile (ACN) was purchased from Merck KGaA, hydrogen peroxide (H_2O_2, purity 35%) was purchased from Merck KGaA, and hydrochloric acid (HCl, purity 37%) was purchased from Carlo Erba Reagents S.r.l. All the solutions were prepared using ultrapure water (Milli-Q® systems, Merck KGaA, Darmstadt, Germany).

The solvothermal synthesis of WO_3 nanoflake powders followed the procedure described by Spagnoli *et al.*[15] The precursor solution was prepared by dissolving 1.25 g of H_2WO_4 in 10 ml of 35% w/w H_2O_2 and 10 mL of ultrapure water under continuous stirring in a beaker placed in a water bath maintained at 95 °C. In total, 18 ml of this H_2WO_4 solution (0.25 M) plus 3 ml of HCl (6 M) and 1.2 g of $H_2C_2O_4 \cdot 2H_2O$ were mixed in 15 ml of ultrapure water and 60 ml of acetonitrile. The precursor solution was subsequently placed in a 1 L Teflon-lined stainless-steel autoclave and heated in an oven at 180 °C for 2 h. After cooling the autoclave to RT, the WO_3 powder was recovered from the Teflon reactor, dried in an oven at 60 °C for few hours, and finally calcined in air for 2 h in a muffle oven at 500 °C.

5.2. Functional material active site characterization

TPR experiments were carried out using a lab-made apparatus with 5% H_2/Ar gas mixture (40 mL min^{-1}). H_2 uptake was monitored using a Gow-Mac thermal conductivity detector (TCD). 100 mg of

 This journal is © The Royal Society of Chemistry 2026

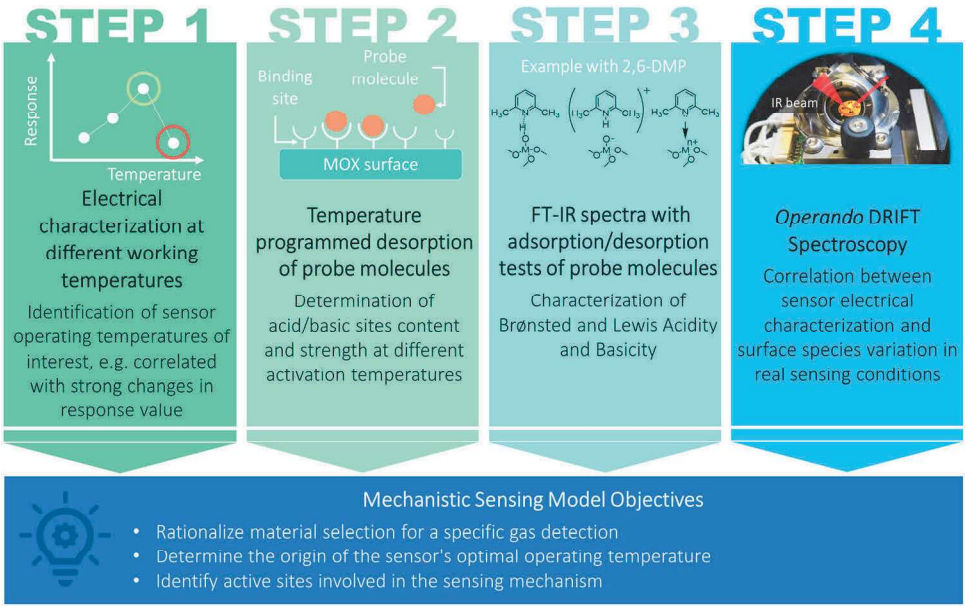


Fig. 8 Experimental workflow for mechanistic elucidation of gas sensing.

the sample were loaded in a quartz reactor and flushed with a mixture of H_2 (5%)/Ar from 25 to 900 °C, at a rate of 10 °C min^{-1}.

TPD analyses were performed using the same lab-made apparatus. The sample (50 mg or 100 mg) was first treated with He flow (30 mL min^{-1}) at 50, 200 or 300 °C for 1 h to remove adsorbed impurities. After cooling to room temperature or to 50 °C, CO_2 or NH_3 (30 mL min^{-1}) was adsorbed on the catalyst sample for 1 h. Finally, the sample was heated to 900 °C at a heating rate of 10 °C min^{-1} in He gas (30 mL min^{-1}) to proceed with the CO_2 (or NH_3) TPD. CO_2 (or NH_3) consumption was measured using a TCD.

FTIR spectra were recorded using a Bruker Vector22 spectrometer equipped with an MCT detector at a resolution of 4 cm^{-1} (128 scans). The solid samples, in the form of self-supported pellets ($\approx$10 mg cm^{-2}), were inserted into a conventional quartz vacuum cell equipped with KBr windows connected to a glass vacuum line (residual pressure $<10^{-5}$ Torr) that allows to perform *in situ* probe molecule adsorption/desorption runs. Samples were activated at either 200 °C or 300 °C in a mild oxidizing environment. Adsorption/desorption tests of 2,6-DMP (to assess the total – Lewis and/or Brønsted – surface acidity[28] of the WO_3 system) were carried out at ambient temperature: a relatively large amount of 2,6-DMP ($\sim$4 Torr) was allowed on the samples and left in contact for 2 min to reach a complete monolayer of the adsorbate; then, the 2,6-DMP excess was evacuated at increasing times in the 1–15 min range to put into evidence only the more strongly held fraction(s). Differential spectra were obtained by subtracting the spectra of thermally activated catalysts from the spectra obtained after adsorption/desorption runs so as to give a semi-quantitative meaning to the FTIR results.

5.3. Sensor fabrication

The WO_3-based gas sensor was prepared by using the commercially attractive and low-cost screen-printing process. The technique of deposition relied on the production of a paste based on the synthesized nanostructured powder with the addition of alpha-terpineol, ethyl cellulose, and ceramic frit, to provide the appropriate viscosity for its deposition and to aid the temperature-induced film treatments.[5] The paste containing the nanostructured WO_3 powder and the additives was sonicated in an Elmasonic S 120 H unit to obtain the desired homogeneity.

The paste was then printed through a AUREL C920 screen printer with a predefined shape (an area of 1.22 × 1.60 mm^2 and a thickness of about 20–30 μm) onto alumina substrates equipped with two interdigitated gold electrodes to supply the input voltage and extract the output signal. First, the film was dried at 150 °C for 4 h to remove the volatile organic compounds. Second, the films were fired at 500 °C for 2 h in a muffle oven to complete the decarbonation process and sinter of the semiconducting layer. The two-step procedure produced a homogenous and compact film by limiting cracks. On the substrate backside, a platinum screen-printed heater was placed to set the operating temperature for sensor thermal activation. The interdigitated gold electrodes and the heater were interfaced to the electronic system by connecting them with golden wires (a diameter of 0.06 mm) to the pins of a commercially available TO39 support through a wedge wire bonder.

5.4 DRIFT spectroscopy and electrical characterization setup

The sensing capabilities of the WO_3-based gas sensor were investigated using a customized apparatus (Fig. S11) including a customized gas test chamber and an interface board for the sensor electrical characterization placed inside the sample compartment of a Vertex 70 IR spectrometer (Bruker).[75] The set-up enabled *operando* studies by providing mid-IR spectroscopic characterization of the sensing film in real time and under working conditions, while also reading out the device's electrical behaviour.

The spectrometer was equipped with Harrick's Praying Mantis mirror optics to work in the DRIFT configuration. A liquid nitrogen-cooled MCT detector was used to record time-resolved spectra. The optics bench and sample compartment were both evacuated to 2 hPa in order to prevent any absorption interference caused by ambient CO_2 and water vapor along the beam path. The WO_3 sensing film was aligned with the IR beam using a vacuum compatible precision XY micro-stage coupled with the *Z*-axis control system. DRIFT spectra were recorded in the range of 4500–800 cm^{-1}, with a resolution of 4 cm^{-1} and an average of 1024 scans. The IR spectra were processed *via* Bruker's OPUS software. To determine the differences in the material surface resulting from changes in the environmental gaseous composition, absorbance spectra were calculated as apparent absorbance (AB) using eqn (1):

$$AB(\lambda) = -\log_{10}\frac{I_{\text{sample}}(\lambda)}{I_{\text{background}}(\lambda)} \quad (1)$$

where $I_{\text{background}}(\lambda)$ is the intensity of the spectrum single channel (SC) of the sensing film recorded under initial experimental conditions, and $I_{\text{sample}}(\lambda)$ is the intensity recorded after a system condition variation, such as an increase in sensor operating temperature or in the gaseous chamber composition. To make the spectra clearer, smooth signal processing and baseline subtraction were applied using Origin (OriginLab). OriginLab was also used for the peak deconvolution and integration. AB raw spectra (Fig. S12–S14) are shown in the supporting information file for the sake of completeness. They evidenced an increasing baseline, which has been observed in previous works from the literature on *operando* DRIFT spectroscopy applied to chemoresistive gas sensors[76,77] and that can be explained by the increase of charge carriers in the MOX films.[5,78]

A schematic diagram of the overall setup and specifications about the test gas chamber and electronics are provided in ref. 5, 75 and 79. The resistance of the sensor was obtained as the ratio of the applied voltage *vs.* the current. The current was acquired continuously, while the applied voltage was fixed at 3 V. Then, the sensor response was defined as:

$$\text{Response} = \frac{(R_{\text{air}} - R_{\text{gas}})}{R_{\text{gas}}} \quad (2)$$

where R_{air} is the film resistance in dry air, while R_{gas} is the film resistance during exposure to the analyte. The relative uncertainty of the sensor response was estimated to be ~0.3%, obtained by propagation of the current measurement accuracy (0.2%)[75] and the intrinsic resistance fluctuations of the WO_3 film (0.05%), assuming independent contributions. The response time was defined as the time required for the sensor signal to reach 90% of its total change upon exposure to D-limonene ($t_{90_response}$), whereas the recovery time was defined as the time required for the signal to return to 10% of its total change after analyte removal ($t_{10_recovery}$). Since the analyte concentration was increased stepwise (0.5–8 ppm), the response time was determined from the dynamic response to 0.5 ppm D-limonene, whereas the recovery time was determined from the dynamic response to 8 ppm D-limonene.

Along with the gas sensor, the test chamber housed a commercially available Sensirion SHT3X sensor for temperature and relative humidity monitoring.

5.5. Experimental details and working conditions

The electrical and IR spectroscopic characterization of the WO_3 films in the present work was performed at sensor working temperatures of 200 °C and 300 °C. Based on previous investigations,[25] the sensor displayed the highest response value *vs.* D-limonene at 200 °C and the lowest at 300 °C. These temperatures were therefore chosen to understand the origin of the sensor's optimal operating temperature.

The sensor characterization was performed using N_2, dry synthetic air, and D-limonene (target gas) coming from certified cylinders to the test chamber. Their fluxes were set through a pneumatic system based on Brooks SLA5800 mass-flow controllers (the error limit of rate is equal to 1%). The total continuous flow rate was maintained at 100 sccm (standard cubic centimeters) throughout all the experiments. During D-limonene sensing measurements, the flow containing the defined concentration of target gas was obtained by mixing two fluxes, one from a dry synthetic air cylinder and one from a cylinder containing D-limonene in a 10 ppm concentration with a relative uncertainty of 2.0% (given from the producer). Eqn (3) was used to calculate the flow rate F coming from the D-limonene cylinder to be set to obtain a total flow of 100 sccm with a D-limonene concentration in the range of 0.5–8 ppm. The parameters in eqn (3) are the total flow rate F_{tot} (100 sccm), the desired D-limonene concentration C, and the analyte concentration in the cylinder C_c (10 ppm).

$$F = \frac{F_{\text{tot}}C}{C_c} \quad (3)$$

Humidified synthetic air for evaluating the influence of H_2O on the surface chemistry of WO_3 and its reactivity *vs.* D-limonene was obtained by fluxing a part of the dry air flux through a bubbler filled with deionized water kept at RT.

NO_2 was used as a probe molecule to further investigate the nature of surface-active sites. A concentration of 3 ppm was achieved by mixing the dry synthetic air flux with a flow from a cylinder containing NO_2 at a concentration of 9 ppm, with a relative uncertainty of 2.0% (given by the producer).

Author contributions

Conceptualization: E. S.; data curation: E. S., A. R., E.G., M.S., A.G., and G.C.; formal analysis: E. S., E. G., and A. G.; investigation: E. S., A. R., E. G., M. S., A. G., G. C., and A. I.; methodology: E. S.; project administration: E. S.; resources: V. G., M. S., S. C., and B. F.; supervision: E. S. and B. F.; validation: E. S.; visualization: E. S.; writing – original draft: E. S.; writing – review & editing: A. R., V. G., E. G., M. S., A. G., G. C., S. C., and B. F.

This journal is © The Royal Society of Chemistry 2026

Conflicts of interest

The authors declare no conflicts of interest.

Data availability

The supporting data and experimental information for this article have been included in the supplementary information (SI). The supplementary information includes additional material characterization (SEM, H_2-TPR, CO_2-TPD), sensor response levels, peak fitting and correlation analyses of *operando* DRIFTS spectra, *operando* DRIFTS characterization under NO_2, and acetone exposure, details of the operango gas test chamber, and additional raw and processed DRIFTS spectra. See DOI: https://doi.org/10.1039/d6tc01511e.

Acknowledgements

Arianna Rossi and Barbara Fabbri acknowledge POR FSE 2014/2020 – Regione Emilia-Romagna. Anna Ianniello acknowledges the PNRR project DM 117 2023 for funding her PhD. Barbara Fabbri and Stefano Caramori also acknowledge support from the PNRR MUR project ECS_00000033_ECOSISTER.

Notes and references

1 U. Weimar and N. Barsan, *J. Electroceram.*, 2001, **7**, 143–167.
2 A. Ponzoni, C. Baratto, N. Cattabiani, M. Falasconi, V. Galstyan, E. Nunez-Carmona, F. Rigoni, V. Sberveglieri, G. Zambotti and D. Zappa, *Sensors*, 2017, **17**, 714.
3 N. A. Isaac, I. Pikaar and G. Biskos, *Microchim. Acta*, 2022, **189**, 196.
4 A. Marikutsa, M. Rumyantseva, E. A. Konstantinova and A. Gaskov, *Sensors*, 2021, **21**, 2554.
5 E. Spagnoli, M. Valt, A. Gaiardo, B. Fabbri and V. Guidi, *Nanomaterials*, 2023, **13**, 2708.
6 P. P. Ortega, S. Gherardi, E. Spagnoli, B. Fabbri, N. Landini, C. Malagù, C. Macchi, C. M. Aldao, M. A. Ponce, A. Z. Simões and E. Longo, *Sens. Actuators, B*, 2025, **440**, 137921.
7 E. Tavaglione, E. Spagnoli, M. Valt, P. Bernardoni, M. Della Ciana, F. Bottegoni, M. Negri, F. Scali, C. Zucchetti, M. Ferroni, M. Ardit, L. Vanzetti, V. Cristino, F. Di Benedetto and B. Fabbri, *Sens. Actuators, B*, 2025, **444**, 138504.
8 M. Epifani, *Sensors*, 2022, **22**, 2247.
9 X. Li, L. Fu, H. Karimi-Maleh, F. Chen and S. Zhao, *Heliyon*, 2024, **10**, e27740.
10 M. Modak, S. Rane and S. Jagtap, *Bull. Mater. Sci.*, 2023, **46**, 28.
11 S. R. Sriram, S. Parne, V. S. C. S. Vaddadi, D. Edla, P. Nagaraju, R. R. Avala, V. Yelsani and U. B. Sontu, *Sens. Rev.*, 2021, **41**, 406–424.
12 G. Lei, C. Lou, X. Liu, J. Xie, Z. Li, W. Zheng and J. Zhang, *Sens. Actuators, B*, 2021, **341**, 129996.
13 D. Bonardo, N. L. W. Septiani, F. Amri, Estananto, S. Humaidi, Suyatman and B. Yuliarto, *J. Electrochem. Soc.*, 2021, **168**, 107502.
14 H. Long, W. Zeng and H. Zhang, *J. Mater. Sci.: Mater. Electron.*, 2015, **26**, 4698–4707.
15 E. Spagnoli, S. Krik, B. Fabbri, M. Valt, M. Ardit, A. Gaiardo, L. Vanzetti, M. Della Ciana, V. Cristino, G. Vola, S. Caramori, C. Malagù and V. Guidi, *Sens. Actuators, B*, 2021, **347**, 130593.
16 T. Vogt, P. M. Woodward and B. A. Hunter, *J. Solid State Chem.*, 1999, **144**, 209–215.
17 B. Gerand, G. Nowogrocki, J. Guenot and M. Figlarz, *J. Solid State Chem.*, 1979, **29**, 429–434.
18 T. Lin, X. Lv, S. Li and Q. Wang, *Sensors*, 2017, **17**, 2779.
19 T. Wen, W. He, Q. Nie, Z. Gong, D. Li, L. Wen and H. Peng, *Sens. Actuators, B*, 2023, **385**, 133687.
20 P. Anandakumar, S. Kamaraj and M. K. Vanitha, *J. Food Biochem.*, 2021, **45**, e13566.
21 A.-T. H. Mossa, *J. Environ. Sci. Technol.*, 2016, **9**, 354–378.
22 H. Wang, Q. Lu, X. Chen, Y. Qian, B. Qian and H. Tan, *Naunyn-Schmiedeberg's Arch. Pharmacol.*, 2024, **398**(5), 5491–5507.
23 A. T. Güntner, S. Abegg, K. Königstein, P. A. Gerber, A. Schmidt-Trucksäss and S. E. Pratsinis, *ACS Sens.*, 2019, **4**, 268–280.
24 I. C. Weber, D. N. Oosthuizen, R. W. Mohammad, C. A. Mayhew, S. E. Pratsinis and A. T. Güntner, *ACS Sens.*, 2023, **8**, 2618–2626.
25 A. Rossi, E. Spagnoli, F. Tralli, M. Marzocchi, V. Guidi and B. Fabbri, *Sensors*, 2023, **23**, 6291.
26 D. Vermaire, *J. Catal.*, 1989, **116**, 309–317.
27 A. J. McCue, G. A. Mutch, A. I. McNab, S. Campbell and J. A. Anderson, *Catal. Today*, 2016, **259**, 19–26.
28 C. Morterra, G. Cerrato and G. Meligrana, *Langmuir*, 2001, **17**, 7053–7060.
29 G. Ramis, C. Cristiani, A. S. Elmi, P. Villa and G. Busca, *J. Mol. Catal.*, 1990, **61**, 319–331.
30 F. Can, X. Courtois and D. Duprez, *Catalysts*, 2021, **11**, 703.
31 F. S. Tehrani, H. Ahmadian and M. Aliannezhadi, *Mater. Res. Express*, 2020, **7**, 015911.
32 S. Zhuiykov and E. Kats, *Nanoscale Res. Lett.*, 2014, **9**, 401.
33 A. Marikutsa, L. Yang, M. Rumyantseva, M. Batuk, J. Hadermann and A. Gaskov, *Sens. Actuators, B*, 2018, **277**, 336–346.
34 A. Staerz, A. Kobald, T. Russ, U. Weimar, A. Hémeryck and N. Barsan, *ACS Appl. Electron. Mater.*, 2020, **2**, 3254–3262.
35 S. M. Kanan, Z. Lu, J. K. Cox, G. Bernhardt and C. P. Tripp, *Langmuir*, 2002, **18**, 1707–1712.
36 R. Balzer, V. Drago, W. H. Schreiner and L. F. D. Probst, *J. Braz. Chem. Soc.*, 2014, **25**(11), 2026–2031.
37 M. J. Madou and S. R. Morrison, *Chemical Sensing with Solid State Devices*, Elsevier, 1989.
38 A. Gurlo, *ChemPhysChem*, 2006, **7**, 2029–2226.
39 D. Kohl, *Sens. Actuators*, 1989, **18**, 71–113.
40 A. Staerz, U. Weimar and N. Barsan, *Sens. Actuators, B*, 2022, **358**, 131531.
41 A. Gurlo, *ChemPhysChem*, 2006, **7**, 2041–2052.
42 B. Junker, X.-X. Wang, U. Weimar and N. Bârsan, *J. Phys. Chem. C*, 2025, **129**, 9795–9800.

43 S. Cichosz and A. Masek, *Materials*, 2020, **13**, 2552.
44 E. A. Schmitt, M. Krott, M. Epifani, K. Suematsu, U. Weimar and N. Barsan, *J. Phys. Chem. C*, 2024, **128**, 1633–1643.
45 K. I. Hadjiivanov, *Catal. Rev.*, 2000, **42**, 71–144.
46 R. V. Mikhaylov, A. A. Lisachenko, B. N. Shelimov, V. B. Kazansky, G. Martra and S. Coluccia, *J. Phys. Chem. C*, 2013, **117**, 10345–10352.
47 Z. Cheng and C. S. Lo, *ACS Catal.*, 2012, **2**, 341–349.
48 S. H. Alrefaee and A. W. Apblett, *Heliyon*, 2019, **5**, e02780.
49 D. G. Barton, S. L. Soled and E. Iglesia, *Top. Catal.*, 1998, **6**, 87–99.
50 W. R. Gunther, V. K. Michaelis, R. G. Griffin and Y. Román-Leshkov, *J. Phys. Chem. C*, 2016, **120**, 28533–28544.
51 P. Y. Dapsens, C. Mondelli and J. Pérez-Ramírez, *Chem. Soc. Rev.*, 2015, **44**, 7025–7043.
52 G. R. Johnson and A. T. Bell, *J. Catal.*, 2016, **338**, 250–264.
53 R. Zhang, J. Jagiello, J. F. Hu, Z.-Q. Huang, J. A. Schwarz and A. Datye, *Appl. Catal., A*, 1992, **84**, 123–139.
54 A. B. Boffa, C. Lin, A. T. Bell and G. A. Somorjai, *Catal. Lett.*, 1994, **27**, 243–249.
55 R. Kourieh, S. Bennici, M. Marzo, A. Gervasini and A. Auroux, *Catal. Commun.*, 2012, **19**, 119–126.
56 K. P. McKenna, *J. Am. Chem. Soc.*, 2013, **135**, 18859–18865.
57 A. Staerz, S. Somacescu, M. Epifani, T. Kida, U. Weimar and N. Barsan, *ACS Sens.*, 2020, **5**, 1624–1633.
58 M. F. Daniel, B. Desbat, J. C. Lassegues, B. Gerand and M. Figlarz, *J. Solid State Chem.*, 1987, **67**, 235–247.
59 R. J. Sáenz-Hernández, G. M. Herrera-Pérez, J. S. Uribe-Chavira, M. C. Grijalva-Castillo, J. T. Elizalde-Galindo and J. A. Matutes-Aquino, *Coatings*, 2022, **12**, 1727.
60 K. Thummavichai, N. Wang, F. Xu, G. Rance, Y. Xia and Y. Zhu, *R. Soc. Open Sci.*, 2018, **25**, 171932.
61 E. C. Hakimeh Pakdel, V. Galstyan, V. Golovanov, A. D'Arco, T. Mancini, F. Mura, M. Rossi, S. Lupi, A. Mezzi and S. Kaciulisg, *J. Mater. Chem. A*, 2025, **12**, 28243.
62 A. Patra, K. Auddy, D. Ganguli, J. Livage and P. K. Biswas, *Mater. Lett.*, 2004, **58**, 1059–1063.
63 B. B. Nayak, T. Dash and S. Pradhan, *J. Electron Spectrosc. Relat. Phenom.*, 2020, **245**, 146993.
64 A. Tocchetto and A. Glisenti, *Langmuir*, 2000, **16**, 6173–6182.
65 C. P. T. Sofian and M. Kanan, *Curr. Opin. Solid State Mater. Sci.*, 2007, **11**, 19–27.
66 S. Americo, E. Pargoletti, M. I. Trioni, R. Soave, F. Cargnoni, G. L. Chiarello and G. Cerrato, *Electrochim. Acta*, 2021, **371**, 137611.
67 A. Rossi, B. Fabbri, E. Spagnoli, A. Gaiardo, M. Valt, M. Ferroni, M. Ardit, S. Krik, A. Pedrielli, L. Vanzetti and V. Guidi, *ACS Appl. Mater. Interfaces*, 2023, **15**(28), 33732–33742.
68 A. Yang, L. Marikutsa, A. Rumyantseva, M. Konstantinova, E. Khmelevsky and N. Gaskov, *Sensors*, 2019, **19**, 3405.
69 M. D'Andria, M. Yin, S. Neuhauser, V. G. Mavrantzas, Y. Chen, K. Suzuki and A. T. Güntner, *Adv. Mater.*, 2026, e16840.
70 D. R. Miller, S. A. Akbar and P. A. Morris, *Sens. Actuators, B*, 2014, **204**, 250–272.
71 I. Weyrauch, E. Louisa Hefler, R. Breuch, P. Kaul, S. Mathur and K. Konstantynovski, *Phys. Status Solidi A*, 2026, **223**, e202400633.
72 Y. D. X. Yang, Y. Deng, H. Yang, Y. Liao, X. Cheng, Y. Zou and L. Wu, *Adv. Sci.*, 2022, **10**, 2204810.
73 Y. C. D. Zhang, J. Wu and P. Li, *J. Mater. Chem. A*, 2017, **5**, 20666–20677.
74 D. X. Xiaoyang Duan, W. Zhao, R. Yan, Y. Xiao, T. Yu, X. Zhao and X. Gong, *Coord. Chem. Rev.*, 2026, **563**, 218011.
75 M. Della Ciana, M. Valt, B. Fabbri, P. Bernardoni, V. Guidi and V. Morandi, *Rev. Sci. Instrum.*, 2021, **92**, 074702.
76 T. Hakkarainen, E. Mikkola, J. Laperre, F. Gensous, P. Fardell, Y. Le Tallec, C. Baiocchi, K. Paul, M. Simonson, C. Deleu and E. Metcalfe, *Fire Mater.*, 2000, **24**, 101–112.
77 M. Pfeiffer and C. Hess, *J. Phys. Chem. C*, 2022, **126**, 3980–3992.
78 D. A. Panayotov and J. T. Yates, *Chem. Phys. Lett.*, 2005, **410**, 11–17.
79 M. Valt, M. Della Ciana, B. Fabbri, D. Sali, A. Gaiardo and V. Guidi, *Sens. Actuators, B*, 2021, **341**, 130012.

 This journal is © The Royal Society of Chemistry 2026